

Electron, Muon, and Hadron Lateral Distributions Measured in Air-Showers by the KASCADE Experiment

T. Antoni^a, W. D. Apel^a, F. Badea^b, K. Bekk^a, K. Bernlöhner^{a,1},
H. Blümer^{a,d}, E. Bollmann^a, H. Bozdog^b, I. M. Brancus^b,
A. Chilingarian^c, K. Daumiller^d, P. Doll^a, J. Engler^a,
F. Feßler^a, H. J. Gils^a, R. Glasstetter^d, R. Haeusler^a,
W. Hafemann^a, A. Haungs^a, D. Heck^a, T. Holst^a,
J. R. Hörandel^{d,2}, K.-H. Kampert^{d,a}, J. Kempa^e, H. O. Klages^a,
J. Knapp^{d,3}, D. Martello^{a,d}, H. J. Mathes^a, H. J. Mayer^a,
J. Milke^a, D. Mühlenberg^a, J. Oehlschläger^a, M. Petcu^b,
H. Rebel^a, M. Risse^a, M. Roth^a, G. Schatz^a, F. K. Schmidt^d,
T. Thouw^a, H. Ulrich^a, A. Vardanyan^c, B. Vulpescu^b,
J. H. Weber^d, J. Wentz^a, T. Wiegert^a, J. Wochele^a,
J. Zabierowski^f

(The KASCADE Collaboration)

^a*Institut für Kernphysik, Forschungszentrum Karlsruhe, 76021 Karlsruhe, Germany*

^b*National Institute of Physics and Nuclear Engineering, 7690 Bucharest, Romania*

^c*Cosmic Ray Division, Yerevan Physics Institute, Yerevan 36, Armenia*

^d*Institut für Experimentelle Kernphysik, University of Karlsruhe, 76021 Karlsruhe, Germany*

^e*Department of Experimental Physics, University of Lodz, 90236 Lodz, Poland*

^f*Soltan Institute for Nuclear Studies, 90950 Lodz, Poland*

¹ Now at: University of Hamburg, Hamburg.

² Present address: University of Chicago, Enrico Fermi Institute, Chicago, IL 60637.

³ Now at: University of Leeds, Leeds LS2 9JT, U.K.

Abstract

Measurements of electron, muon, and hadron lateral distributions of extensive air showers as recorded by the KASCADE experiment are presented. The data cover the energy range from 5×10^{14} eV up to almost 10^{17} eV and extend from the inner core region to distances of 200 m. The electron and muon distributions are corrected for mutual contaminations by taking into account the detector properties in the experiment. All distributions are well described by NKG-functions. The scale radii describing the electron and hadron data best are $\simeq 30$ m and $\simeq 10$ m, respectively. We discuss the correlation between scale radii and ‘age’ parameter as well as their dependence on shower size, zenith angle, and particle energy threshold.

Key words: cosmic rays; air shower; lateral distribution

PACS: 96.40.Pq

1 Introduction

Since the detection of extensive air showers (EAS) [1] lateral or radial density distributions $\rho(r)$ of different kinds of particles produced in EAS have been an ongoing target of experimental as well as theoretical investigations. There are a number of reasons why EAS lateral distributions are of importance for the air shower phenomenon. The first and most important one is that from the number and distribution of ground particles the energy and mass of the primary particle can be deduced. While at least the energy reconstruction can be done rather crudely from analytical considerations, more reliable algorithms need detailed air shower simulations to relate the observables to primary energy and mass. Perhaps trivial, although experimentally very important, is the fact that in measurements the shower particles are always sampled over a limited range of core distances $r_1 < r < r_2$ only – in most cases with an area coverage in this range not much exceeding one percent – but showers are often referred to in terms of integrated numbers of particles:

$$N = \int_{r_1}^{r_2} 2\pi r \rho(r) dr. \quad (1)$$

The total particle numbers, N , for different kinds and energy ranges of shower particles, are obtained by choosing $r_1 = 0$ and $r_2 = \infty$ and are traditionally used both as measures for the primary energy in an individual experiment as well as a means for comparison of different experiments. Comparing experimental results is generally hampered by different detector characteristics like energy thresholds and discrimination of particle types but also by different

observation altitudes. These effects need to be corrected, e.g. using suitable air shower and detector response simulations.

Detector effects are, in principle, minimized by disentangling the lateral distributions (and thus also the total particle numbers) for various kinds of particles. For experiments using a single type of detector this is generally not an option and resulting lateral distributions correspond to some mixture of different particle types, depending on the detection technique used as well as on absorber thicknesses and thresholds applied. Experiments with several detector components optimized for different particle types still measure a mixture of particles, but are able to disentangle various types to a large extent. The present paper follows this path to obtain lateral distributions separately for the major charged particles – electrons, muons, and hadrons – in EAS of primary energies from 5×10^{14} eV up to almost 10^{17} eV.

Integrating from $r_1 = 0$ to $r_2 = \infty$ implies an extrapolation beyond the core distance ranges actually covered. Deviations of measured lateral distributions from the expected form, as a consequence, result in systematic errors of the particle numbers obtained. Such systematic errors can be very much reduced by using ‘*truncated*’ particle numbers integrated only over the experimentally covered range of core distances. This approach is introduced for muons in section 3.1. The main drawback of such truncated particle numbers is that comparisons of different experiments are further complicated.

The lateral distribution functions also carry information on the related particle physics and astrophysics. Different hadronic interaction models predict different lateral shapes. Hence, it is possible to test available interaction models. Unfortunately, from a particle physicists point of view, the expected lateral shape also depends on the mass of primary cosmic rays. Heavier primaries lead, on average, to a flatter distribution. Since the lateral distribution is only one in a group of composition-sensitive observables measured with KASCADE, no attempts are made to infer any mass parameter in the present paper. This will be addressed in a separate article.

Historically, choices of parametrizations of both electron and muon lateral distributions were influenced very much by the seminal review of Greisen [2]. Greisen described the lateral density function (*LDF*) of the electromagnetic (*e.m.*) component of EAS by

$$\rho_{\text{em}}(r, N_e) = \frac{0.4N_e}{r_M^2} \left(\frac{r_M}{r}\right)^{0.75} \left(\frac{r_M}{r+r_M}\right)^{3.25} \left(1 + \frac{r}{11.4r_M}\right) \quad (2)$$

over the core distance range from $r = 5$ cm to $r = 1500$ m and for atmospheric depths of 537 g/cm² to 1800 g/cm². The parameter N_e is the total number of electrons in the shower and r_M is the Molière radius. The Molière unit, about

0.25 radiation lengths in air, characterises the spread of low-energy electrons by multiple scattering.

Greisen also noted that Eq. 2, except for the last factor, is a close approximation to the analytical calculations for electromagnetic showers performed by Kamata and Nishimura [3] if a shower *age parameter* of $s = 1.25$ is assumed. Greisen's approximation to the Nishimura-Kamata functions for $0.5 < s < 1.5$ is referred to as the NKG function:

$$\rho_{\text{NKG}}(r, s, N_e) = \frac{N_e}{r_M^2} \frac{\Gamma(4.5 - s)}{2\pi\Gamma(s)\Gamma(4.5 - 2s)} \left(\frac{r}{r_M}\right)^{s-2} \left(1 + \frac{r}{r_M}\right)^{s-4.5}. \quad (3)$$

This function, often used to describe the charged particle lateral distribution, will in the following be applied individually to electron, muon, and hadron distributions by choosing appropriate sets of parameters (s, r_M) . For a comparison of the parametrization of Kamata and Nishimura with the NKG function (Eq. 3) see [4].

Many experimental groups reported deviations of the e.m. LDF from the NKG form which are most obvious at large core distances [5–7]. This may be related to the problem that the NKG form has originally been formulated for *zero* energy threshold of shower electrons in purely electromagnetic showers and that higher moments of the NKG form tend to diverge, depending of the age parameter s . More general forms were, for example, suggested by Hillas and Lapikens [8] and Capdevielle et al. [9].

Traditionally, the NKG form is used with a fixed value of r_M and a variable age parameter s . Thus, the scale length is kept constant while the shape of the LDF is assumed to be variable. A different LDF and a scaling relation were proposed by Lagutin et al. [10], based on Monte Carlo calculations for pure electromagnetic showers. They proposed a normalized LDF $f(x)$ with

$$xf(x) = \exp(-3.63 - 1.89 \ln x - 0.370 \ln^2 x - 0.0168 \ln^3 x), \quad (4)$$

independent of primary energy and age at least in the range $0.05 \leq x \leq 25$, where x is the core distance divided by a scale radius, here the root mean square (rms) radius, $\sqrt{\langle r^2 \rangle}$, of the particle density at ground. Note that Eq. 4 has finite higher order moments but is not useful for small x .

Greisen [2] also suggested a functional form for the muon LDF in EAS

$$\rho_\mu(r, N_\mu) = \text{const.} \cdot N_\mu \left(\frac{r}{r_G}\right)^{-\beta} \left(1 + \frac{r}{r_G}\right)^{-2.5}, \quad (5)$$

with $\beta = 0.75$, now referred to as the Greisen function. In the original form, which was based on a very limited number of events, the Greisen radius r_G is 320 m. This form refers to a minimum muon energy of 1 GeV but a more general form for the 1–20 GeV range was also quoted by Greisen. Deviations of the muon LDF from the Greisen form (Eq. 5) were reported by several experimental groups, such as [11–13]. Alternatives were suggested by Linsley [14] and by Hillas et al. [15]. The KASCADE experiment allows to scrutinize the muon LDF for different thresholds (0.23–2.4 GeV), although only for core distances below 100–230 m.

For the hadronic (originally termed *nuclear interacting* or just *N*) component, the LDF depends very much on the hadron energy, with more energetic hadrons being more concentrated near the shower core. This was already pointed out by Greisen [2].

Hadron lateral distributions were investigated by previous experiments mainly close – within 10 m or less – to the shower core. Rather wide lateral distributions measured at Tien Shan initiated speculations on rising mean values of transverse momenta or on strongly rising cross-sections of jet production [16]. At Chacaltaya hadrons far away from the shower axis and with high values of $p_T \approx 2$ GeV/c have been observed [17]. Similar discrepancies between observations and calculations were reported repeatedly, e.g. by the Turku group, claiming an increase of large transverse momentum processes with rising energy (see [18] and references therein). Features suggesting strong changes in the characteristics of hadronic interactions in the PeV range were also claimed in [19,20].

Early parametrizations of the hadron LDF assumed a power law form, as for instance shown in the review by Cocconi [21]. More recently, Maket-ANI reported agreement with exponential forms within 5 m from the core [22]. The Chacaltaya group found a NKG-like function to fit their lateral distribution best for core distances up to 10 m [23]. The KASCADE hadron calorimeter with its large detection area and large dynamic range not only provides better statistics but also allows to extend the hadron LDF analysis to much larger core distances than any previous experiment.

2 The KASCADE experiment

The KASCADE (*KArlsruhe Shower Core and Array DEtector*) experiment is located at Forschungszentrum Karlsruhe, Germany, at an altitude of 110 m a.s.l. and has been described in detail in [24,25]. The experiment has three major components: an array of electron and muon detectors, a central detector mainly for hadron measurements but with substantial muon detection areas,

and a tunnel with streamer tube muon telescopes. Since the latter have only been completed at the time of writing this article, no data from the muon tunnel are included in the present analysis.

The KASCADE array covers an area of about $200 \times 200 \text{ m}^2$ and consists of 252 detector stations located on a square grid of 13 m separation. These are organized in 16 clusters of 16 stations each, except for the inner four clusters where the location of one station is blocked by the central detector. The stations contain two types of detectors, liquid scintillation counters (e/γ detectors) of 0.79 m^2 area each and 5 cm thickness with little shielding above and plastic scintillators of 0.81 m^2 area each and 3 cm thickness (muon detectors) below a shielding of 10 cm lead and 4 cm steel. The inner four clusters are instrumented with four e/γ detectors per station but without muon detectors while the outer 12 clusters house two e/γ and four muon detectors per station. For both detector types the sum of photomultiplier signals, the earliest time, and the hit pattern are recorded for all stations fired.

The central hadron calorimeter is of the sampling type and has a fiducial area of $16 \times 19 \text{ m}^2$. A detailed description can be found in [26]. The energy is absorbed in an iron stack and sampled in eight layers of liquid ionization chambers with anode segments of $0.25 \times 0.25 \text{ m}^2$ (appr. 38 500 channels). The thickness of the iron slabs increases from 12 to 36 cm towards the deeper parts of the calorimeter, amounting to 154 cm in total. The 8th layer is located below an additional concrete ceiling of 77 cm thickness. On top, a 5 cm lead layer filters off the soft electromagnetic component. The ionization chambers are read out by logarithmic amplifiers and 13 bit ADCs, achieving a dynamic range of 6×10^4 . Signals starting from single minimum ionizing muons up to energy deposits of 10 GeV in a chamber are read out without saturation. The response curve of each channel is calibrated with a reference capacitor coupled to the preamplifier, injecting known charges into the electronics chain.

Below the 8th calorimeter layer, two layers of multiwire proportional chambers (MWPCs), vertically separated by 38 cm, are used as muon detectors. In total, 32 chambers are operated with 129 m^2 total area per layer. Hits are registered on anode wires and two layers of cathode strips at angles of $\pm 34^\circ$ with respect to the wires.

A total of 456 plastic scintillation counters of $0.48 \times 0.95 \text{ m}^2$ area each and 3 cm thickness are used within the calorimeter (below 5 cm lead and 36 cm steel) to trigger the calorimeter and the MWPCs. They also serve as muon counters. On top of the calorimeter, an additional 50 such counters fill the central gap of e/γ detectors but their data are not included in the present analysis. A summary of the detector components used in this article together with their most relevant parameters is given in Table 1.

Table 1

KASCADE detector components used in this analysis. Detection thresholds refer to particle energies above the absorber material of the detectors.

Detector	channels	separation	total area	threshold E_{kin}	for
array e/γ	252	13 m	490 m ²	5 MeV	e
array μ	192	13 m	622 m ²	230 MeV $\times \sec \theta$	μ
trigger	456	—	208 m ²	490 MeV $\times \sec \theta$	μ
MWPCs	26 080	—	129 m ²	2.4 GeV $\times \sec \theta$	μ
calorimeter	38 368	—	304 m ²	50 GeV	hadrons

3 Data analysis procedures

3.1 Shower reconstruction

Shower parameters are reconstructed from the array data in a procedure with three iterations. In a first step core positions are obtained by the centre of gravity (*COG*) of the e/γ detector signals. The shower direction is determined assuming a plane shower front. In this first step, the electron and muon shower sizes, N_e and N_μ , are obtained by summing up the relevant detector signals of the e/γ and muon detectors, respectively, and multiplying them with a core-position dependent geometrical weight factor. Next, the shower direction is obtained by fitting a conical shower front to the recorded times of e/γ detectors which are within 70 m from the shower core. The core position is fitted simultaneously with the electron shower size and the electron lateral shape parameter. Next, the e/γ detector signals are corrected for expected contributions from particles other than electrons, and muon detector signals are corrected for expected electromagnetic and hadronic punch-through (see Section 3.2). The main differences between the second and third iteration are improved corrections. Signals largely inconsistent with those in the neighbouring detectors or with expected fluctuations of particle numbers, or signals more than some 200 ns off from the shower front are discarded in this fit. This greatly reduces the impact of hadronic and electromagnetic punch-through on muon signals.

In the shower reconstruction, both the electron and muon lateral distributions are assumed to follow a NKG form with a Molière radius of 89 m and 420 m, respectively. For muons, the fit is performed by considering only detector stations at core distances between 40 and 200 m. The *truncated muon size*, N_μ^{tr} , is then defined by integrating Equation 1 in this range. The lower integration limit is imposed by severe punch-through near the shower axis and the upper one is approximately the largest core distance of any counter for showers

with their cores inside KASCADE. The scale radius of 420 m and the *muon age* parameter s_μ were deduced from simulations. The latter can not be fitted on a shower-by-shower basis due to limited statistics. Therefore, it is derived from CORSIKA simulations [27] and parametrized as a function of N_e . The actual values are obtained by fitting CORSIKA muon density distributions individually for proton and iron induced showers and taking the mean value of both parametrizations. This leads to a mass dependent systematic error in the reconstruction of N_μ^{tr} in a range of up to 5 % but yields a more robust result than trying to fit also s_μ on a shower-by-shower basis.

The actual muon LDF is known to deviate from the assumed NKG form outside the fit range. Within the limited range accessible to the experiment, the NKG form is nevertheless, on a shower-by-shower basis, as good as the Greisen function or any other form with suitably adapted parameters. Simulations show that N_μ^{tr} provides a very good estimate of the primary energy, almost independent of the primary particle mass [28].

The adopted electron LDF is also known to deviate from experimental data at large core distances, even though the age parameter is fitted on a shower-by-shower basis for core distances of 10–200 m. This results in an underestimate of N_e up to 5–8% for simulated showers.

The core position can be reconstructed with an uncertainty of about 3 m at 1 PeV, and the accuracy is typically better than 1 m for showers above 4 PeV if the core is located well inside the array. In order to use data of best quality, the analysis of average lateral distributions in this paper is restricted to showers with core positions within 91 m from the centre of the array. The angular resolution for such showers above 1 PeV is about 0.4° (68 % C.L.). Statistical sampling errors on N_e (N_μ^{tr}) improve from about 10% (20%) at 1 PeV to about 3% (10%) at 10 PeV.

3.2 Particle numbers in array detectors

The signal analysis of the e/γ detectors takes account of muons by subtracting their expected energy deposits from the measured energy. In the same way, the expected e/γ and hadron punch-through contributions are subtracted from the energy deposit in the muon detectors. Since both are mutually related, an iterative procedure is applied. Finally, the number of particles hitting a detector is estimated by dividing the remaining energy deposit by the expected energy deposit per particle. There are no means to discriminate against hadrons in the array detectors.

In total, the procedure requires four *lateral energy correction functions* (LECFs) which are, in the most general case, a function of core distance, zenith angle,

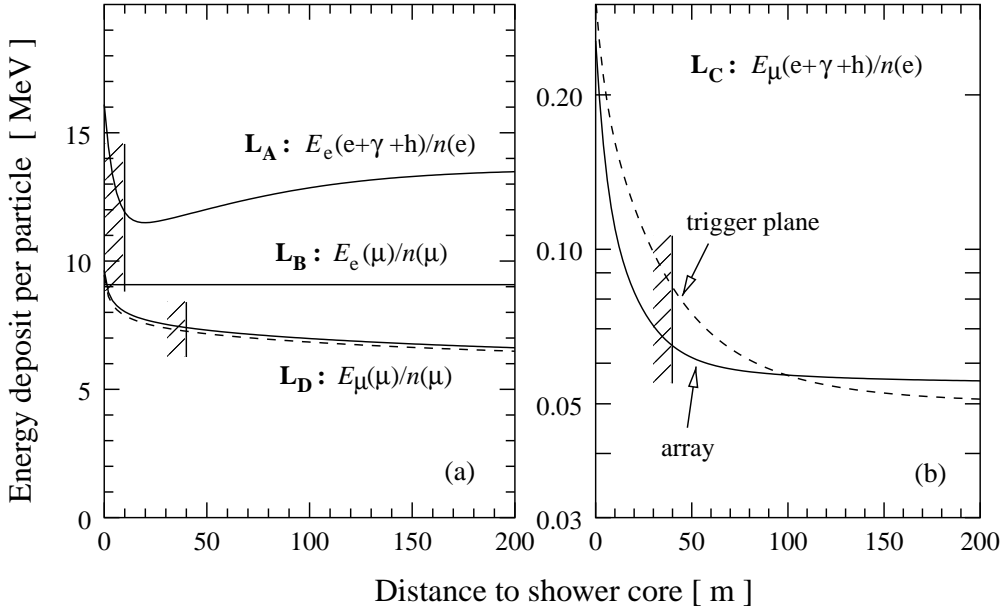


Fig. 1. Parametrized lateral energy correction functions as used in the analysis of average LDFs. Left: L_A and L_B for deposits in the array e/γ counters (see text) and L_D for muons in array muon counters (solid line) and trigger plane counters (dashed line). Right: Punch-through corrections (evaluated for $N_e = 10^5$) for array muon and trigger plane counters, corresponding to final likelihood cuts used to reject counters with far too large energy deposits. Correction functions left of the hatched lines are only shown for illustration but not used in the shower reconstruction.

and shower size. Actually, there is a weak dependence on the cosmic-ray mass composition, too. Hence, mean values of the LECFs for simulated proton and iron primaries are used. All LECFs were obtained from CORSIKA simulations of EAS (using the QGSJET model [29]) followed by detailed detector simulations (based on the GEANT package for detector simulation [30]). The same event reconstruction is applied to simulated as to experimental data. As a result, the energy deposits can be related to the numbers and types of particles hitting the detectors. For the analysis of average lateral distributions special refined LECF functional forms are used (see Fig. 1). They do not change fundamental shower parameters like N_e or N_μ^{tr} , but improve the reproduction of the average lateral distribution of simulated showers. LDFs obtained after detector simulation and shower reconstruction closely match LDFs of the relevant particle type and energy threshold before detector simulation.

The following correction functions are used: L_A is the average sum of energy deposits by electrons, gammas, and hadrons in the e/γ counters normalized to the number of electrons above 5 MeV kinetic energy, $n(e)$, hitting the counter; L_B is the average energy deposit by muons in the e/γ counters per muon; L_C is the average punch-through energy deposit of electrons, gammas, and hadrons in the muon counters per electron; L_D is, in turn, the average deposit of muons in the muon counters per muon. The average energy deposits $E_{e\gamma}$ and E_μ in

e/γ and muon detectors, respectively, are:

$$E_{e\gamma} = A_{e\gamma}(L_A\rho_e + L_B\rho_\mu)$$

and

$$E_\mu = A_\mu(L_C\rho_e + L_D\rho_\mu),$$

with $A_{e\gamma}$ and A_μ being the areas of the detectors and ρ_e and ρ_μ the particle densities. Parametrized correction functions are given in Fig. 1. The rise of L_A at small and large core distances is due to hadrons and gammas, respectively. L_D rises at small distances because of energetic knock-on electrons released by high-energy muons in the absorber material above the muon counters.

L_A and L_B are adjusted for the core distance range 10–200 m, and L_C and L_D for the range 40–200 m. For core distances below 20–40 m the electromagnetic and hadronic punch-through, even on average, exceeds the energy deposit by muons in the muon counters. Despite the reduction of ‘spikes’ and correction for other punch-through, systematic errors on the muon LDF due to punch-through remain significant below 40 m core distance. For this reason, the array muon analysis was restricted to core distances farther than 40 m.

The expected numbers of the ‘wrong’ particle types in the second and third iteration are derived from the fitted lateral distributions of the previous step. Therefore, to some extent the derived shower sizes depend on the assumed shapes. The electron size N_e , in particular, depends on the extrapolation of the assumed electron LDF to radii below 10 m and above 200 m, as well as on the assumed muon LDF at radii below 40 m – the latter resulting in about 2% systematic error.

After shower reconstruction lateral distributions of average energy deposits are obtained for various bins of shower size and zenith angle. A similar procedure to the one described above is applied to correct for the contribution of other particle types, but now on the *average* and not individual energy deposits. Therefore, refined LECFs are used to get average particle density distributions. Again, the corrections for muons in the e/γ detectors and for electron punch-through into the muon detectors are calculated iteratively, by using LDFs from the preceding iteration. In each iteration, both electron and muon LDFs are fitted and the slope s_μ of the muon LDF is no longer parametrized (see Sec. 3.1) but is fitted as well. In these fits, we take into account not only the statistics of hits but also the uncertainty expected in the punch-through correction and we consider effects caused by the experimental resolution in determining the core position.

3.3 *Muon numbers in the trigger plane*

The trigger plane has a muon energy threshold of 490 MeV and, therefore, less electromagnetic punch-through than the array muon detectors. On the other hand, the dynamic range of signals is smaller and hadronic punch-through is more significant because of the outset of cascading in the absorber material above. The effect of hadronic punch-through is reduced by rejecting detector elements within a distance of 1 m to identified high-energy hadrons (typically above 50 GeV). Further reduction of hadronic and electromagnetic punch-through is achieved by rejecting counters with energy deposits inconsistent with the expected numbers of muons, accounting for statistical number fluctuations and for fluctuations in the energy loss of muons.

Conversion of average energy deposits into particle numbers in the trigger plane closely follows the procedure outlined for the array detectors. LECFs for trigger plane counters were derived from simulations – with the same selection criteria applied as for experimental data. Most notably, the punch-through correction is different for array detectors (Fig. 1b), but the different composition of materials above the muon counters also results in slightly different effective energy loss distributions (Fig. 1a).

3.4 *Reconstruction in the MWPCs*

Hits of single muons in the MWPCs are characterised by signals on one or a few anode wires and an average of 3.5 neighbouring cathode strips on each side. Hit reconstruction requires that the intersection of the two cathode signals coincides with an anode signal. At low particle densities this reconstruction achieves a good efficiency and spatial resolutions are 1.4 cm along wires and 0.7 cm perpendicular. At high densities of about 5 muons/m², signals of several hits start to overlap and ambiguities arise in the reconstruction.

Muon tracks are reconstructed from pairs of hits in the two detector layers. Accepted tracks are required to be in reasonable agreement with the shower direction ($\Delta\theta \leq 15^\circ$; $\Delta\phi \leq 45^\circ$ if $\theta \geq 10^\circ$), which effectively resolves ambiguous hits. Systematic uncertainties in calculating efficiencies are reduced by discarding those muons which, according to the shower direction, could be observed in one layer of the MWPCs only. Thereby, hits near the edges of the chambers are rejected. Furthermore, muons entering from the sides of the building in inclined showers would have a lower than nominal energy threshold. To compensate for this effect, only those areas of the MWPCs are used where muons parallel to the shower directions have penetrated the entire iron absorber of the calorimeter. Geometric and reconstruction efficiencies were ob-

tained from the shower and detector simulation chain followed by the normal reconstruction procedure. The particle detection efficiency in the MWPCs itself is derived continuously by using muons observed in the trigger layer and the other of the two MWPC layers and is typically 98%. All efficiencies are accounted for in the lateral distributions.

3.5 Hadron reconstruction

Briefly, the algorithm for pattern recognition of hadrons in the eight layers of ionization chambers proceeds as follows [26]: Clusters of energy are searched to line up in the calorimeter and to form a track in different layers from which an approximate angle of incidence can be inferred. Then, patterns of cascades are searched for in the deeper layers. Going upwards in the calorimeter, clusters are formed from the remaining energy and are lined up to showers according to the direction already found. The reconstruction efficiency for isolated hadrons is 70% at 50 GeV and reaches nearly 100% at 100 GeV.

Hadron energies are reconstructed from the sum of calibrated signals in layers 2–8, weighting each layer by the relative amount of preceding absorber. The uppermost layer is not used for the energy determination to avoid distortions by electromagnetic punch-through. The weighted signal sum is converted to energies by a function derived from detector simulations based on the GEANT package. The energy resolution is rather constant, slowly improving from 20% at 100 GeV to 10% at 10 TeV.

Due to the fine lateral segmentation of 25 cm, the minimal distance to separate two equal-energy hadrons with a 50% probability amounts to 40 cm. This causes the reconstructed hadron number density to flatten off at about 1.5 hadrons/m². The reconstructed hadron energy density, on the other hand, is not affected by this saturation [26]. Radiation from high-energy muons can mimic hadrons. However, their reconstructed energies are much lower than those of the actual muon, typically by a factor of 10. Simulations show that a 1 TeV muon is identified as a hadron with a probability of about 1% [31].

4 Electron lateral distribution

Average LDFs of electrons have been reconstructed for shower sizes from less than 10⁴ to more than 10⁷ electrons. Contributions of hadrons, muons, and gammas to energy deposits in the e/γ detectors were corrected for by the procedure outlined in Section 3.2. Resulting lateral distributions for electrons above 5 MeV kinetic energy are presented in Fig. 2. NKG functions fit the data

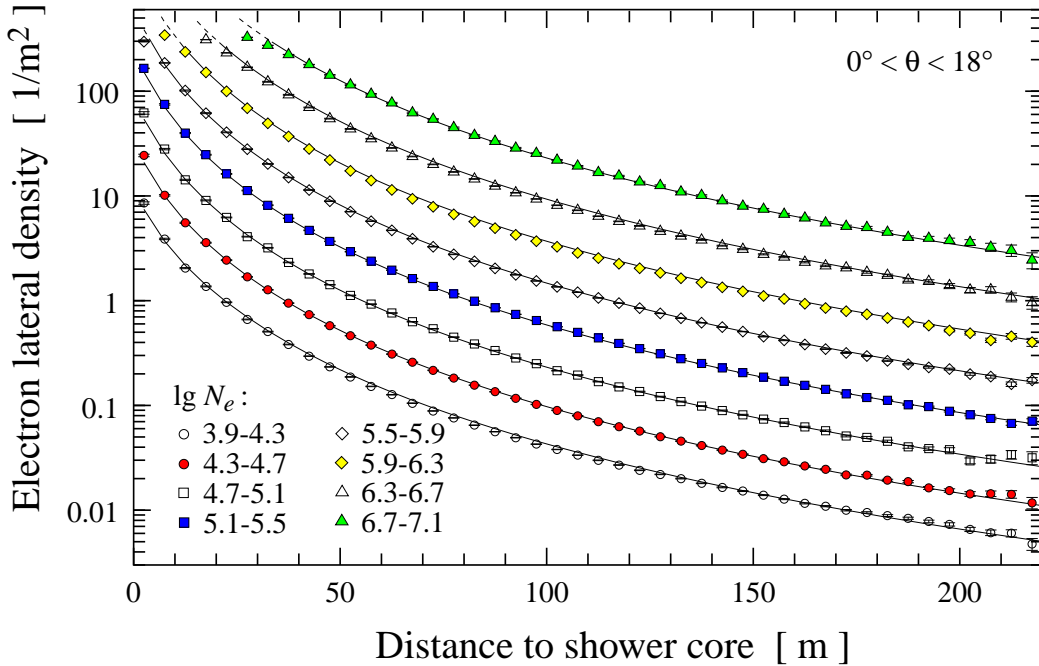


Fig. 2. Lateral distributions of electrons above a 5 MeV kinetic energy for zenith angles below 18° . The lines show NKG functions of fixed age parameter $s = 1.65$ but varying scale radius r_e (see text).

quite well and are represented by lines. Reduced χ^2 values are $\simeq 1-3$ with only the lowest N_e bin being worse by about a factor of 2. Note that saturation effects in *average* lateral distributions become relevant at electron densities of approximately 300 m^{-2} although individual counters have a dynamic range of up to 600 m^{-2} . The effect is attributed to shower-by-shower fluctuations and it does not influence the measurement in individual events.

Deviations of the experimental LDF from the NKG function (Eq. 3) have been discussed in the literature frequently (see Section 1) and are subject to more detailed studies presented below. It turns out that the NKG function *can* describe the KASCADE electron LDF over the core distance range 10–200 m surprisingly well – but the best agreement is achieved with parameters far away from the conventional assumption of $r_M \approx 80 \text{ m}$. When fitting N_e , r_M , and s simultaneously, the measured LDFs can be reproduced at the 1% level for $r_M \approx 20-30 \text{ m}$ and $s \approx 1.6-1.8$. The actual values depend on shower size and zenith angle. In order to avoid confusions with the original Molière radius, r_M , we will call this fit parameter of the electron lateral distributions r_e in the following. Two-parameter fits with conventional r_e are substantially worse, as can be seen in Fig. 3. Similar results have been found in γ -shower calculations by Hillas and Lapikens [8]. In the fits, we find a strong correlation between r_e and s . A corresponding parameter map has been generated by scanning (s, r_e) and fitting N_e . The reduced χ^2 -values are about one and are plotted as black areas in Fig. 4. It seems worth noting that the optimal value of r_e

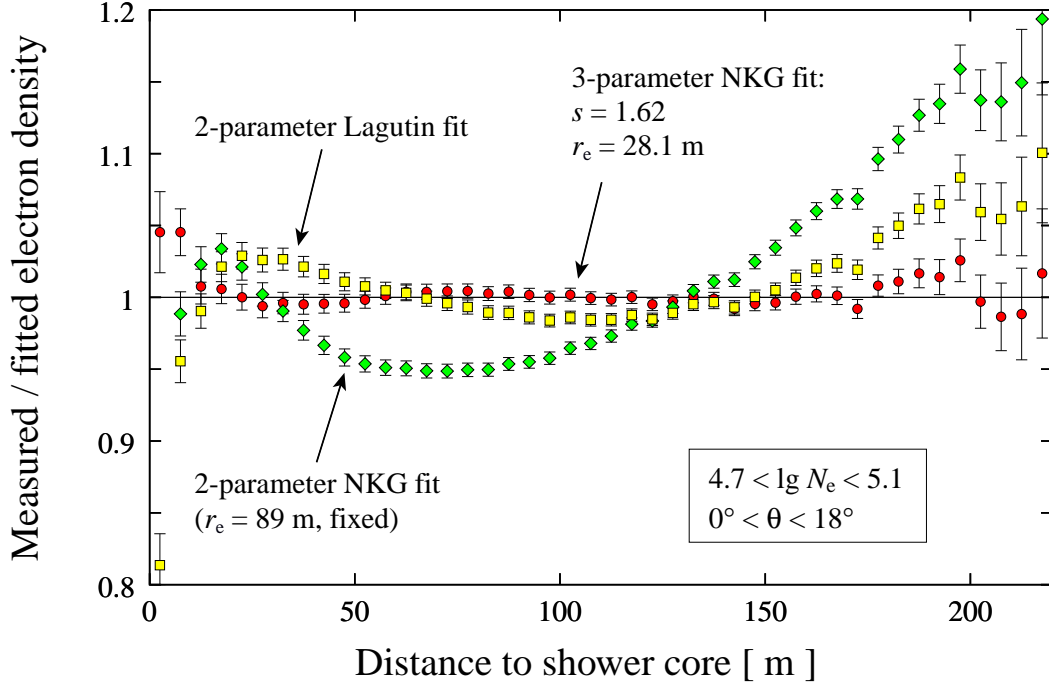


Fig. 3. Residuals in the ratio of measured over fitted average LDF, with the NKG function (3-parameter fit, circles: N_e , r_e and s free; 2-parameter fit, diamonds: r_e fixed at 89 m) and the function (4) proposed by Lagutin [10] (squares; N_e and rms-radius fitted).

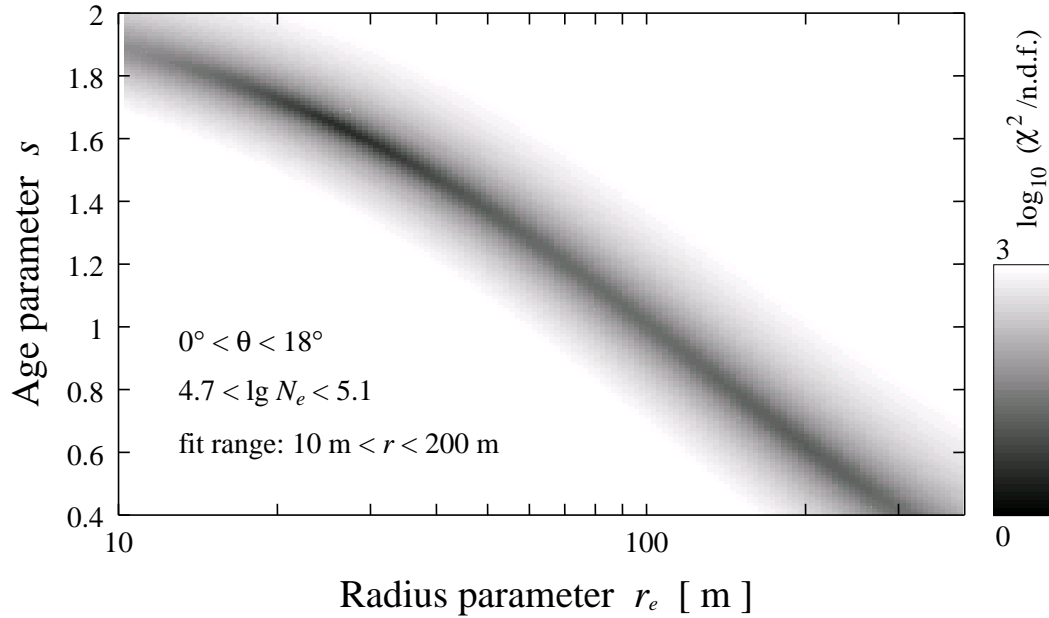


Fig. 4. Logarithm of the reduced χ^2 when fitting the KASCADE average electron lateral distribution by the NKG function, with r_e and s varied over a wide range (only N_e fitted).

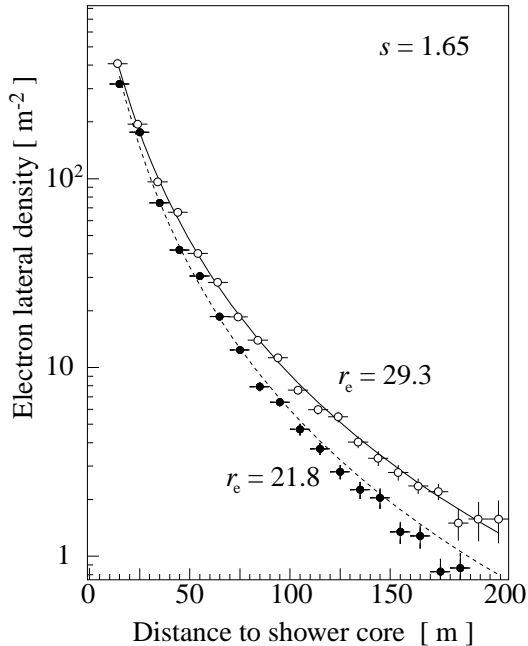


Fig. 5. Lateral distributions of two EAS events as measured by KASCADE. Both distributions are approximated by NKG functions of fixed age parameter $s = 1.65$. The fit parameters are $r_e = 29.3$ m, $N_e = 2.3 \cdot 10^6$ (full line), and $r_e = 21.8$ m, $N_e = 2.0 \cdot 10^6$ (dashed line). The reconstructed zenith angles are $\theta = 26^\circ$ and $\theta = 30^\circ$, respectively.

tends to decrease and of s to increase, both with increasing shower size and with increasing zenith angle. This variation does not exactly follow the ridge shown in the r_e - s plane of Fig. 4.

At the level of accuracy possible in individual showers, the correlation between r_e and s entail highly ambiguous values if r_e and s are fitted simultaneously. Therefore, r_e is usually fixed and the steepness of the lateral distributions is quantified by the fit parameter s . A problem mostly relevant to NKG functions with small scale radii $r_e \simeq 25$ m is, that upwards fluctuations of the large s parameter easily lead to ill defined shower sizes. CORSIKA simulations show, that this problem can be circumvented if s is fixed and r_e fitted, instead. An example of experimental electron lateral distributions of events with similar shower size N_e and zenith angle is presented in Fig. 5. The difference in shape is clearly visible and well accounted for by the different r_e parameters of the fitted NKG functions. The sensitivity of r_e to the primary mass will be subject of a forthcoming publication.

Since evaluation of N_e involves an extrapolation of the LDF beyond the fiducial range, fitting with non optimal r_e causes systematic errors of the shower size obtained. In case of KASCADE, variations of the Molière radius in the range $25 \text{ m} < r_e < 89 \text{ m}$ change N_e by up to 5%. Using a *truncated electron size* in analogy to N_μ^{tr} , no such extrapolation would be required. Since the required

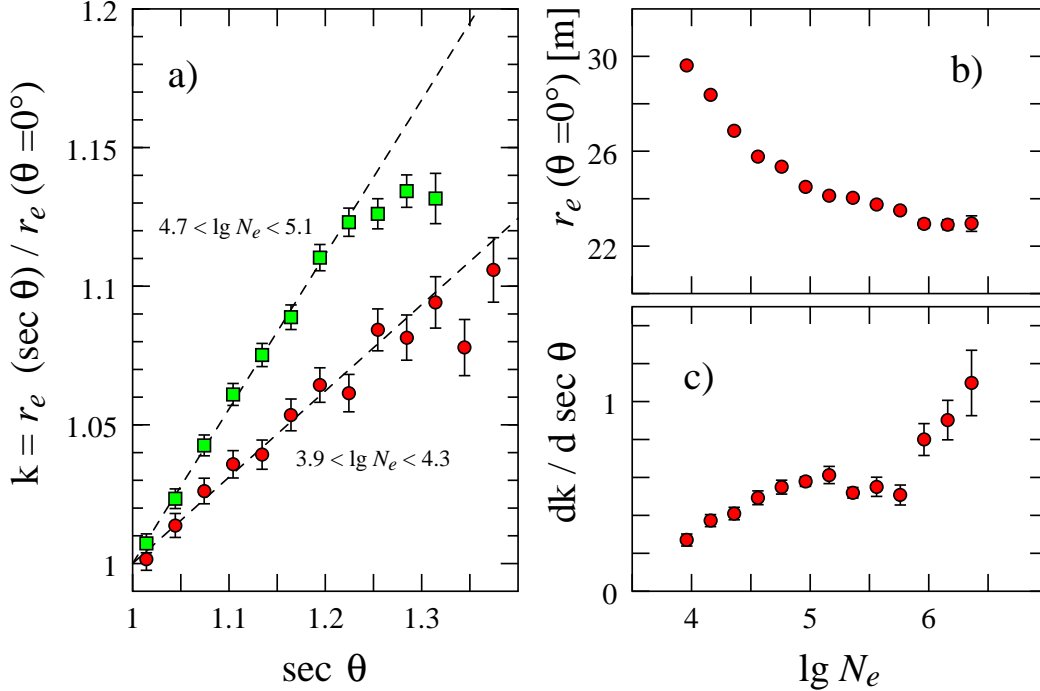


Fig. 6. a) Shower scale radius r_e as a function $\sec \theta$, normalised to the scale radius for vertical showers. The lateral distributions were fitted by NKG functions with $s = 1.65$ fixed. Only showers with $3.9 < \lg N_e < 4.3$ and $4.7 < \lg N_e < 5.1$ have been considered. The dashed lines represent linear fits in the range $1 < \sec \theta < 1.25$. b) Radius parameter r_e for vertical incidence. c) Slope of the linear function fitted as shown in a) as a function of shower size.

correction is fairly small – in contrast to the N_μ case – we keep using a total electron shower size.

Figure 3 shows, in addition to the NKG function, also residuals for a fit with the LDF of Eq. 4 proposed by Lagutin et al. The rather moderate description of the experimental data is not particularly surprising, since Eq. 4 was developed for purely electromagnetic showers. However, this form has a much more reasonable behaviour at large core distances than the NKG form. The rms-radius calculated directly from the experimental data and used by Lagutin et al. as the scale radius, would be diverging when evaluated analytically from our best-fit NKG form. Lagutin et al. also claimed that the shape of the LDF remains unchanged when the radius is expressed in units of a variable scale radius. We tested this scaling hypothesis by fitting electron lateral distributions of different shower sizes and zenith angles to the NKG form and fixing the age parameter to $s = 1.65$, a value which provided the best overall fit for all data considered. Again, the reduced χ^2 is in the range 1–4 with slightly better fits obtained for larger shower sizes. No significant dependence on zenith angle is observed. The parameter r_e of the fits can then be considered the variable scale radius. As shown in Fig. 2, all data can be reproduced rather well – with

the largest deviations seen for shower sizes $3.9 < \lg N_e < 4.3$. This probably is due to selection effects at threshold. For small zenith angles, r_e varies from about 30 m at $N_e = 10^4$ to 24 m at $N_e = 10^6$, with little change beyond that size. A comparison with results from 3-parameter NKG fits to the electron LDF reveals that the scaling assumption does indeed reproduce all our electron data rather well, but residuals of up to $\simeq 5\%$ also demonstrate significant deviations from perfect scaling.

Apart from the scaling for different shower sizes it is particularly illustrative to see a change of the scale radius as a function of zenith angle. To be independent of the scale chosen and the precise form of the LDF used, the scale radius shown in Fig. 6a is normalized to that for vertical showers. Using the Lagutin function instead of NKG, consistent results are obtained. A linear relation between scale radius and the secant of the zenith angle θ is obvious and is mainly a result of the increasing distance between the detector and the shower maximum. Electrons are being scattered away from the shower axis as the shower has to penetrate a larger air mass. The slope in this relation can, in fact, be used to infer the average depth of shower maximum – although additional corrections based on simulations have to be applied. The increase of the depth of shower maximum with increasing shower size, and thus energy, results in a decrease of the scale radius as seen in Fig. 6b. Also, the slope of the normalised scale radius versus $\sec \theta$ rises with shower size (see Fig. 6c). An exception from the otherwise monotonic change is apparent at shower sizes corresponding to the knee in the flux spectrum, which we observe at $\lg N_e = 5.7$ [32]. A quantitative analysis of the phenomenon in terms of possible change of the chemical composition is beyond the scope of this paper.

5 Muon lateral distributions

The KASCADE experiment measures lateral distributions of muons for three different energy thresholds (Table 1). In the following, we group the showers in bins of truncated muon numbers N_μ^{tr} . Punch-through and efficiency corrections are applied as described in Section 3. Ranges of core distances for the different muon energy thresholds are limited by uncertainties in the punch-through corrections at small core distances and by the geometry of the KASCADE detector array. Since N_e/N_μ^{tr} rises with shower size, the impact of punch-through corrections becomes more severe at higher energies and the minimum core distances have to be increased correspondingly. For showers with cores inside KASCADE, the upper limit is about 220 m for array detectors and 100 m for central detector components.

As is well known, the muon LDF at sea level and in the energy range considered in this work is much flatter and typically an order of magnitude lower than the

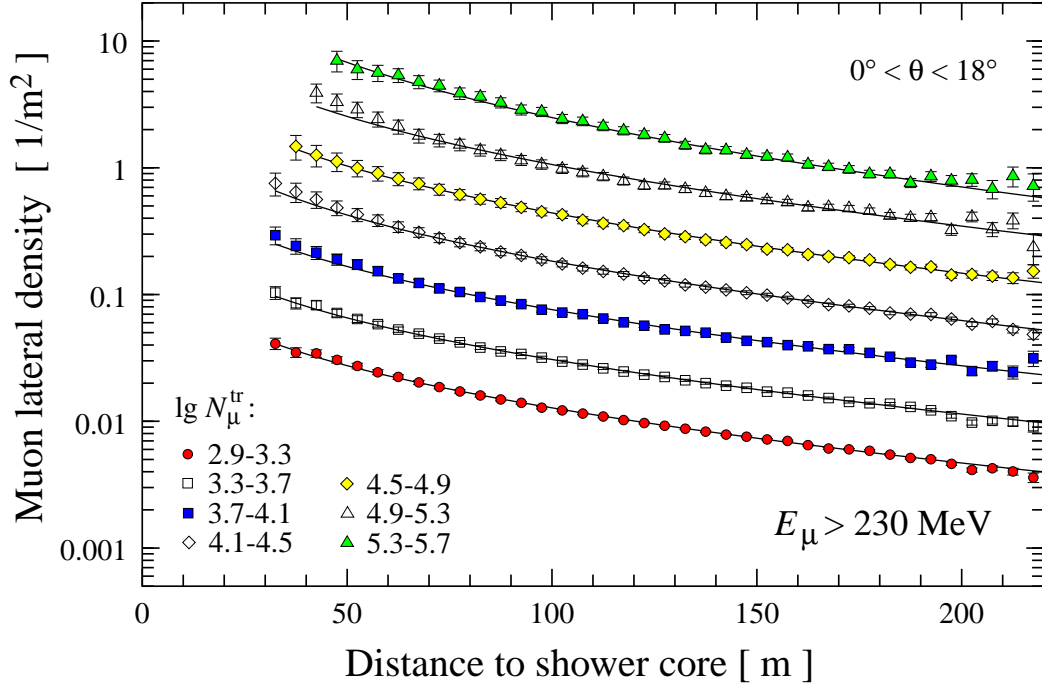


Fig. 7. Lateral distribution of muons above 230 MeV kinetic energy, measured with the array detectors. The lines indicate NKG functions fitted to the data. Error bars are of statistical nature including an uncertainty of 10% on the punch-through correction applied.

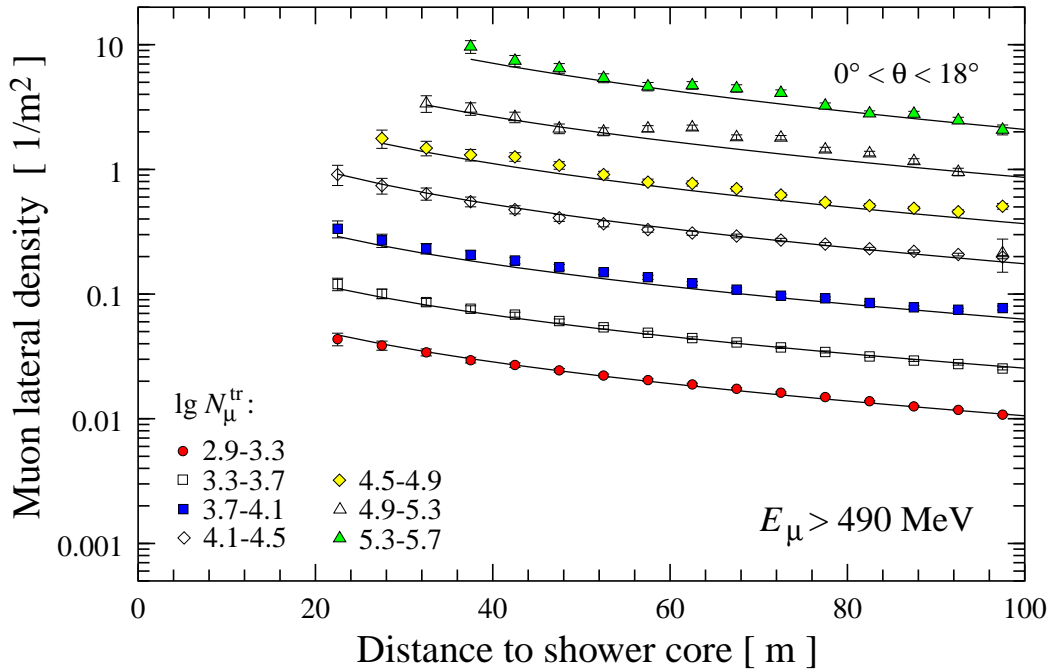


Fig. 8. Lateral distribution of muons above 490 MeV kinetic energy, as measured with the trigger plane. Data are binned according to N_{μ}^{tr} as measured by the array and the lines represent NKG fits to the data.

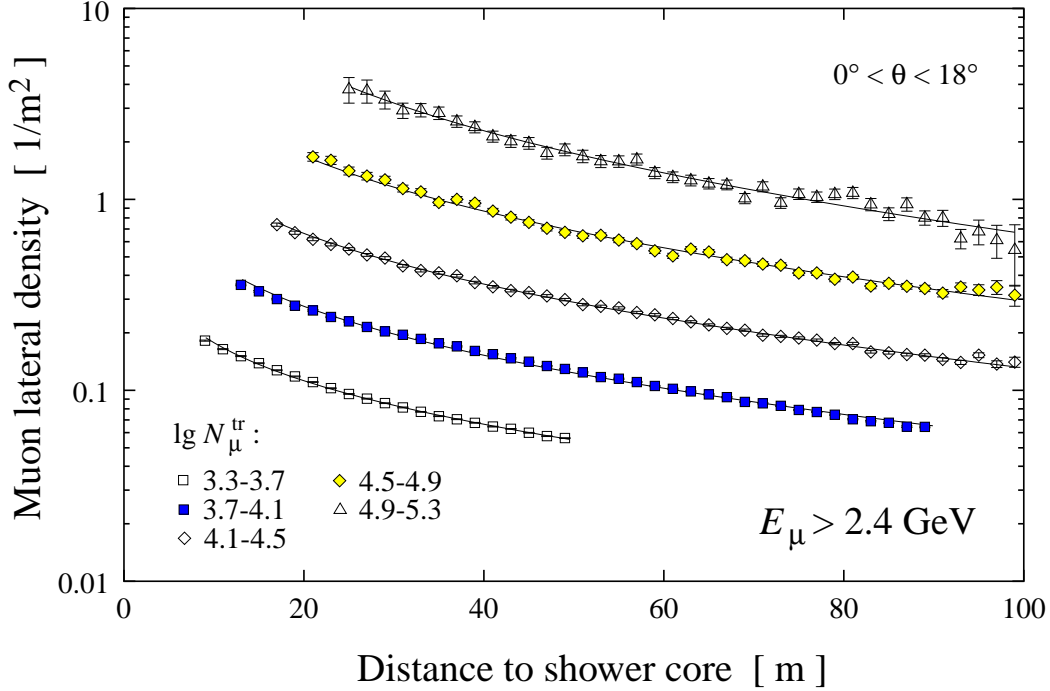


Fig. 9. Lateral distribution of muons above 2.4 GeV kinetic energy. Error bars are statistical only. Data are binned according to N_{μ}^{tr} as measured by the array and the lines represent NKG fits to the data.

electron LDF in our range of core distances. Figure 7 presents average muon lateral distributions with an energy threshold of 230 MeV. NKG functions with $r_{\mu} = 420$ m are superimposed as dashed lines and typically fit the data to better than 5%. The Greisen function (Eq. 5) or the forms suggested by Linsley [14] and by Hillas et al. [15] do not – within the small range of accessible core distances – provide a substantially better description of the data. The rather unconventional application of the NKG form in fitting the muon lateral distribution for individual showers (see Section 3) is, therefore, not expected to affect the quality of the N_{μ}^{tr} measurement. As in the case of electrons (see Fig. 4), the s and r_{μ} values in NKG fits and also the β and r_c values in Greisen fits are highly correlated. While the total number of muons N_{μ} is affected by this ambiguity of the scale radius, N_{μ}^{tr} is not, because no extrapolation beyond the fiducial core distance range is performed.

Muon density distributions above a threshold of 490 MeV as obtained with the trigger plane detectors are presented in Fig. 8. Again, they are equally well fitted by NKG as by Greisen functions. Due to the smaller detector area, statistical errors are larger than for the array muon LDF. Nevertheless, the same range of N_{μ}^{tr} is covered, allowing to compare both muon LDFs. Apart from threshold effects this comparison can serve as an additional check for any systematics, for example due to punch-through corrections or cuts applied which are quite different in both cases.

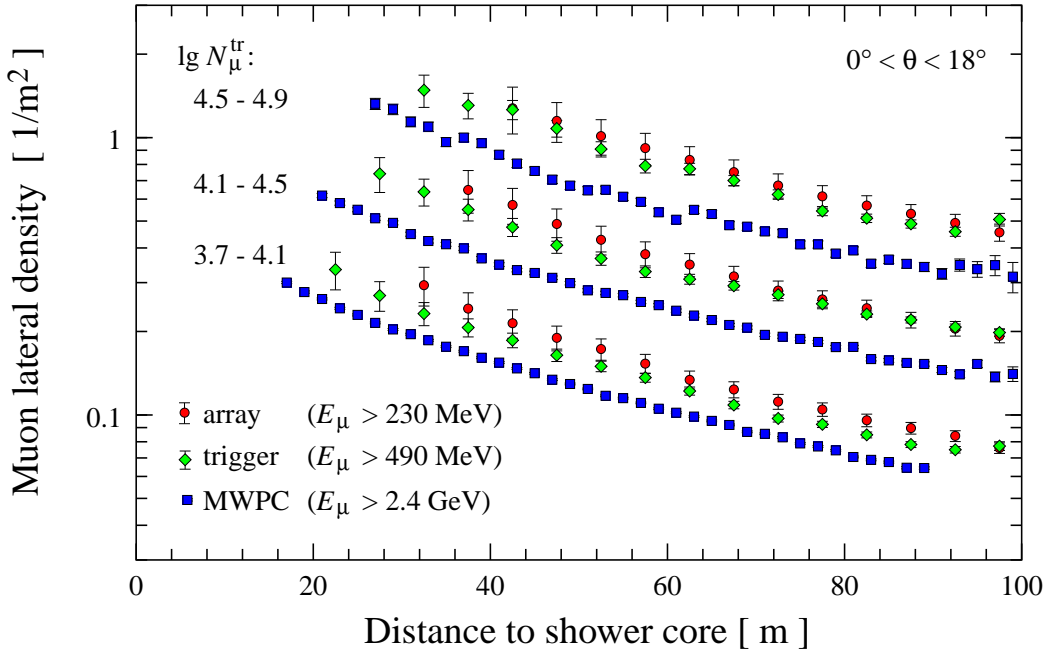


Fig. 10. Comparison of lateral distributions as measured with the different KASCADE detector components, for three different intervals of N_μ^{tr} .

Muons with energies above 2.4 GeV are measured with the MWPC system and their LDF is presented in Fig. 9. Since these detectors are triggered only by the scintillators of the trigger plane and not by the array stations, full efficiency is reached only above the trigger threshold presently set at 7 counters in the trigger plane, i.e. at $\rho_\mu \simeq 0.04 \text{ m}^{-2}$. The chambers identify a muon as a track and no punch-through correction is applied. The lower core distance limit is applied mainly because of hadronic punch-through in EAS cores.

The lateral distributions obtained for the different thresholds are compared in Fig. 10. As expected, the muon density decreases with increasing threshold. The drop of about 10% between 230 and 490 MeV and of about 50% between 230 MeV and 2.4 GeV is nearly independent of primary energy and only weakly dependent on core distance.

For all thresholds, the muon LDF flattens with increasing zenith angle and steepens with increasing shower size (see [33]). This is illustrated in Fig. 11 for muons above 230 MeV, where the age parameter s in NKG functions fitted with a fixed $r_\mu = 420 \text{ m}$ is shown. The observed effect is comparable to that of the electron LDF. With increasing primary energy, i.e. rising N_μ^{tr} , the shower penetrates deeper into the atmosphere resulting in steeper lateral distributions. With increasing zenith angle, in contrast, the shower maximum recedes from the experiment resulting in correspondingly flatter distributions. This is partly compensated by a harder muon spectrum which is due to longer decay path lengths.

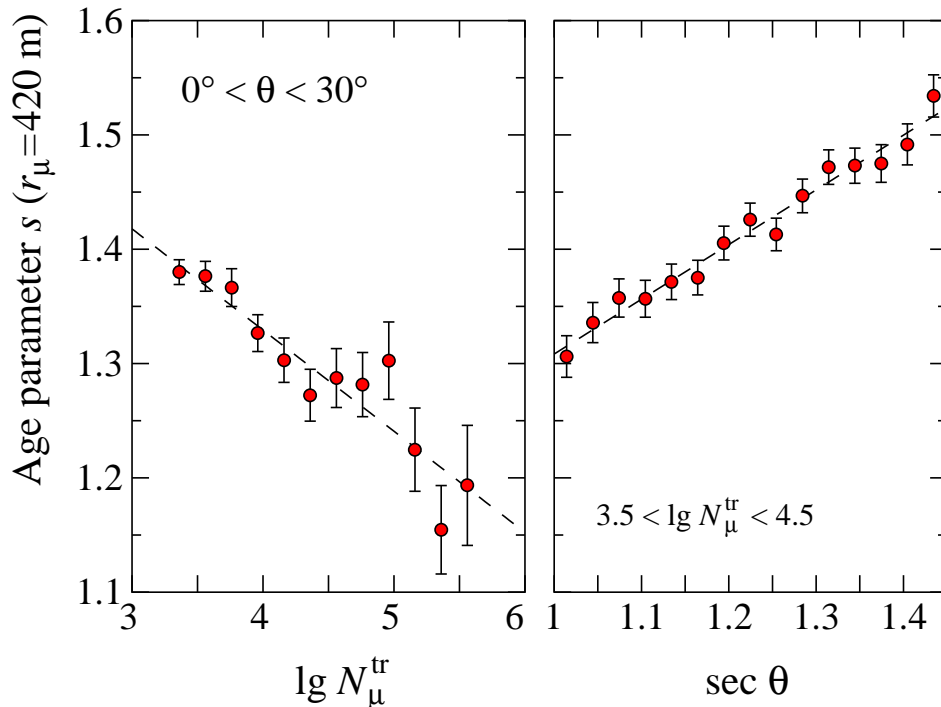


Fig. 11. The age parameter s in NKG fits with fixed $r_\mu = 420$ m for muons of 230 MeV threshold. a) Dependence on N_μ^{tr} , for zenith angles below 30° . b) Dependence on the secant of zenith angle θ , for $3.5 < \lg N_\mu^{\text{tr}} < 4.5$. The dashed straight lines are drawn to guide the eye.

6 Hadron lateral distribution

Data on lateral distributions of hadrons studied over a large range of distances to the shower core are very scarce in the literature [17]. The KASCADE calorimeter operated jointly with the array detectors enables such investigations to be performed with high quality. Different from electrons and muons, the reconstruction of individual energies of hadrons enables to study in detail also the hadronic energy dependence of lateral distributions as well as to compare lateral particle and energy density distributions. As an example, Fig. 12 presents hadron lateral distributions for four N_μ^{tr} sizes corresponding approximately to the energy interval from 1 to 10 PeV. The densities of hadrons and of hadronic energy are given. They extend up to distances of 90 m from the shower core where the intensity has dropped by nearly five orders of magnitude. At the very centre, a saturation as mentioned in section 3.5 can be noticed for the hadron number. Hence, in this range the hadronic energy is the more reliable observable.

Several functions have been applied to fit the data points, among others exponentials suggested by Kempa [34]. However, by far the best fit was obtained when applying the NKG formula represented by the curves shown in the graph.

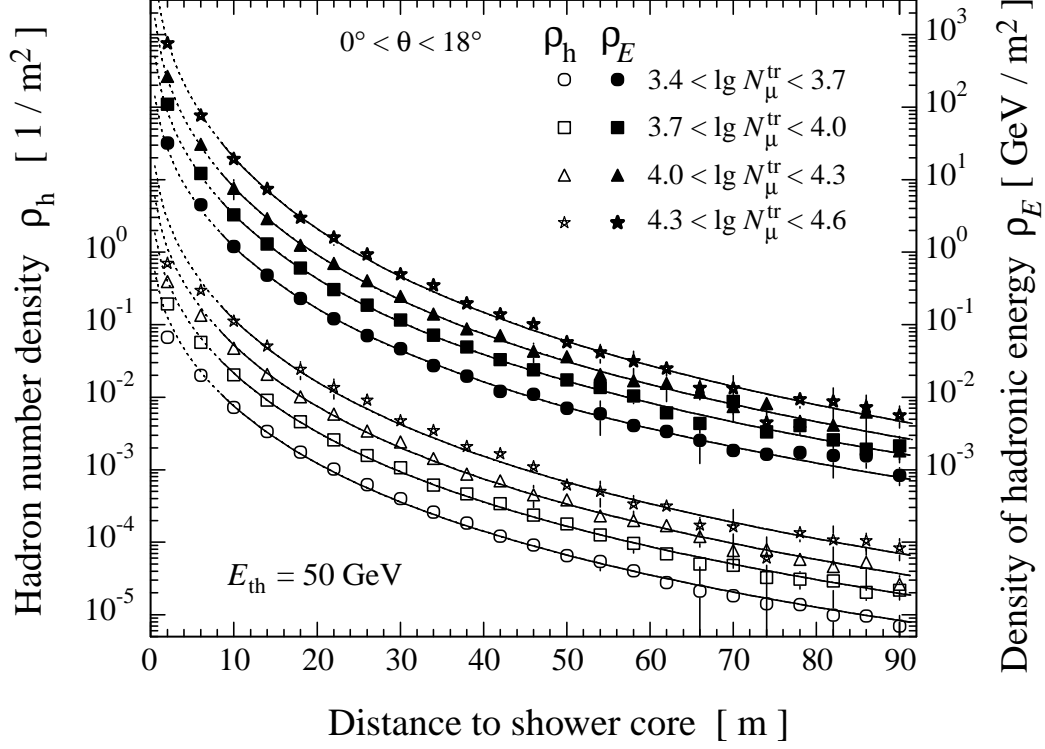


Fig. 12. Density of hadron number (left scale, open symbols) and of hadronic energy (right scale, filled symbols) versus the core distance for showers of truncated muon numbers as indicated. Threshold energy for hadrons is 50 GeV. The curves represent fits of the NKG formula to the data at $r \geq 8$ m with a radius fixed to $r_h = 10$ m.

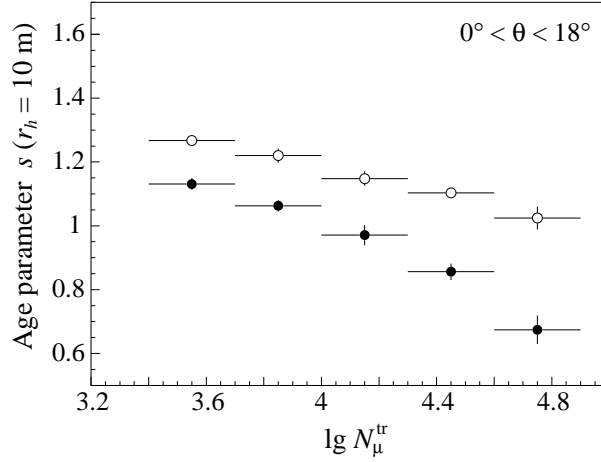


Fig. 13. The age parameter s for fixed radius $r_h = 10$ m versus the muon shower size N_μ^{tr} . Open symbols are for hadronic particle density and full symbols for hadronic energy density.

Because of the mentioned saturation effects close to the shower centre, the actual fit is only applied to the data points within the range of the full lines while the dashed curves are extrapolations to smaller distances. The distributions are much narrower than those of the electrons and the scale radii determined

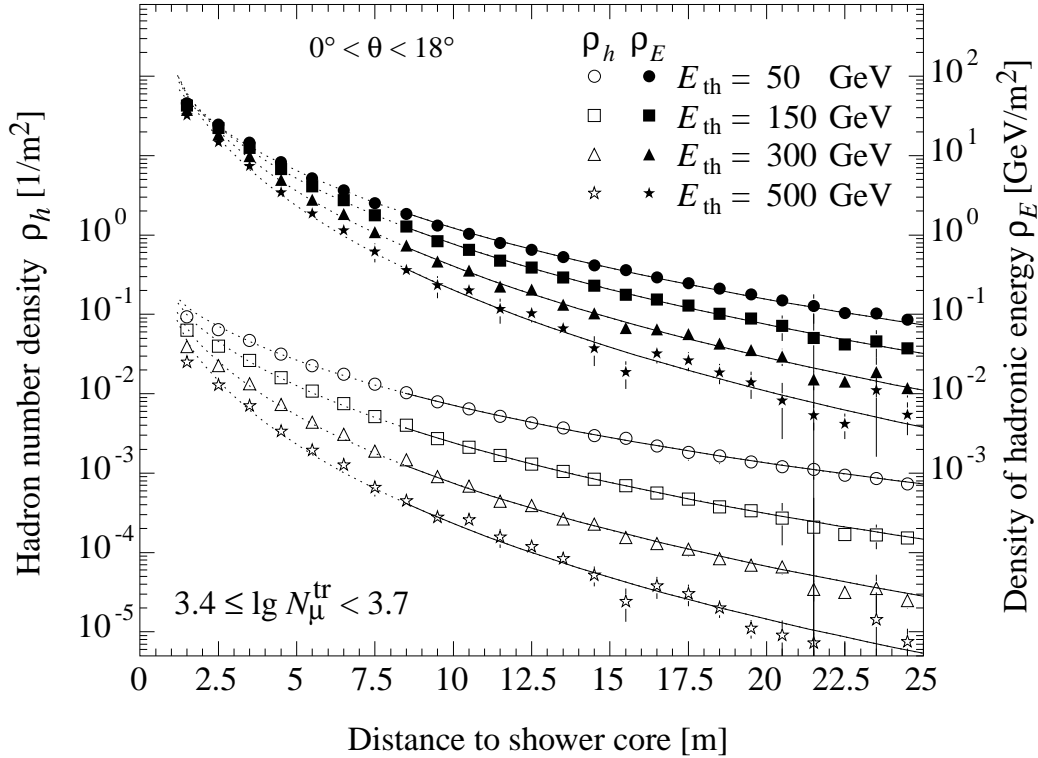


Fig. 14. Density of hadron number (left scale, open symbols) and of hadronic energy (right scale, filled symbols) versus shower core distance for various thresholds of hadron energy. The curves represent fits of the data to the NKG function as in Fig. 12.

by the fit are about $r_h \simeq 10$ m. Furthermore, a variation of the lateral shape is observed which is similarly to that of the electron LDF. When fixing $r_h = 10$ m to determine the age parameters s , we get the result presented in Fig 13. The age parameter yields values similar to the electromagnetic and muonic component and decreases with increasing shower size as expected.

The smaller scale radii and the observed variation with shower size may be interpreted in the picture of high energy hadrons passing through the atmosphere and generating essentially the electromagnetic component. Multiple scattering of electrons then resembles the scattering character of hadrons with a mean transverse momentum of 400 MeV/c almost irrespective of their energy. Hence, in a dimensional estimate of the hadronic lateral scale radius we substitute in the formula of the Molière radius, $r_M = X_0 \cdot E_s/E_c$, the radiation length X_0 by the hadronic interaction length, the scaling energy $E_s = m_e c^2 \sqrt{4\pi/\alpha} \simeq 21.2$ MeV by the mean transverse momentum, and the critical energy E_c (which approximately coincides with the average energy of the electrons at observation level) by the threshold energy of detected hadrons and arrive at a radius $r_h \simeq 1.2 \text{ km} \times 400 \text{ MeV}/50 \text{ GeV} \simeq 10$ m, such as is observed experimentally.

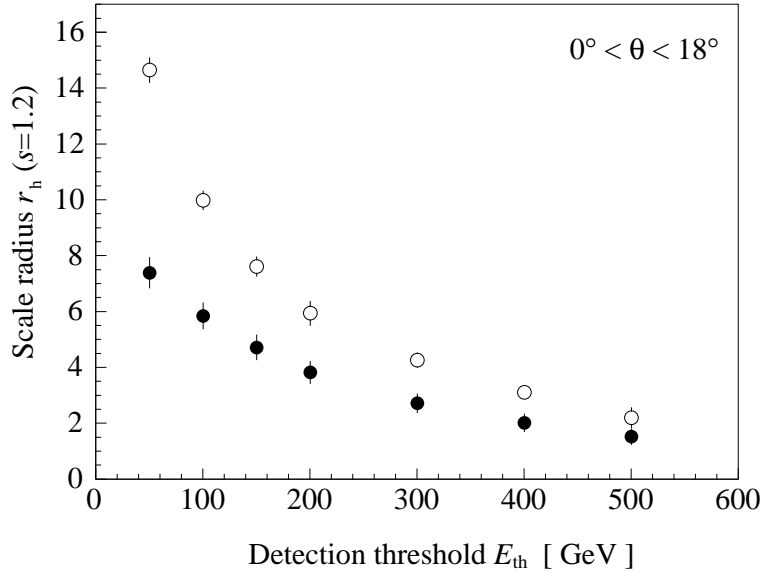


Fig. 15. Hadronic scale radius r_h as a function of detection threshold E_{th} for a fixed shower age of $s = 1.2$ and $3.4 < \lg N_{\mu}^{tr} < 3.7$. Filled symbols are for hadronic energy density and open symbols for hadronic particle density.

Figure 14 provides a closer view to the shower axis for different threshold energies. Again, hadron numbers and energy densities are given. We observe that energetic hadrons are concentrated very close to the centre. The number of TeV hadrons drops by an order of magnitude within the first 3 m. The energy density ρ_E is well described by the NKG formula down to small distances to the shower axis. Deviations at distances up to about 1 m are attributed to the limited core position resolution of the detector. The variation of the hadronic scale radius, r_h , with the detection threshold, E_{th} , applied to the hadrons is displayed in Fig. 15. The data corroborate the expected dependence of the shower width on energy threshold, E_{th} , as outlined above.

7 Summary and Outlook

Measurements of electron, muon, and hadron lateral distributions as recorded by the KASCADE experiment have been presented for radial distances of up to 200 m and for the energy range $5 \times 10^{14} \text{ eV} < E < 10^{17} \text{ eV}$. Detector simulations were performed to account for effects like muon and hadron contamination in signals of the e/γ -scintillators and for punch-through of electrons and hadrons into the muon detectors.

All types of lateral distributions are well described by NKG-functions using different scale radii r_i (with $i = e, \mu, h$) for the different air shower components.

- A study of the electron LDFs shows that optimum fits are not obtained for the canonical value of $r_M = 79$ m, but for $r_e \simeq 20 - 30$ m, i.e. we observe a stronger curvature in the experimental data than in the conventional NKG function. This imposes a systematic effect of up to 5% in the integrated number of shower electrons. Due to the strong correlation of r_e and s , the preferred lower scale radius is accompanied by a larger age parameter of $s \simeq 1.65$. The optimum set of parameters depends on shower size and zenith angle and may be used to infer the mass of the primary particle. For practical reasons and because of limited statistics within single events, information about the shape of the electron LDF is usually extracted by fixing r_e and fitting only the age parameter s . A problem specific to NKG functions in this approach and with small scale radii r_e is, that upwards fluctuations of s easily lead to ill defined shower sizes. As an alternative, we have demonstrated that a fixed age parameter but variable scale radius provides an equally good fit to the data. The parameter r_e then changes in a characteristic way and also exhibits a distinct structure at shower sizes corresponding to the knee position.
- Within the fiducial area of KASCADE, muon LDFs are well described by a NKG function, but with a scale radius of $r_\mu = 420$ m. Because of the limitation to $40 \text{ m} < r < 200 \text{ m}$, the experiment is not very sensitive to the actual value chosen and the data are also equally well described by a Greisen parametrization. Significant differences would only occur at radial distances outside the acceptance of the experiment. The unknown flat shape of the muon LDF at large distances imposes serious problems (even for much larger surface detector arrays) when calculating the total number of muons within an air shower. Most importantly, N_μ is subject to systematic shifts and increased fluctuations, thereby deteriorating the shower size and primary energy resolution. Thus, for classifying events, we have introduced the truncated muon number, N_μ^{tr} , obtained from integrating the LDF only within the experimental acceptance of 40-200 m. A rough scan of the low energy muon spectrum has been performed by analysing LDFs at $E_\mu \geq 230$, 490, and 2400 MeV. Similarly to electrons, a steepening of the muon LDF is observed with increasing shower size and decreasing zenith angle, as is expected for observations being increasingly closer to the shower maximum.
- Quite interestingly, also hadronic lateral energy density and particle number distributions are well approximated by the NKG form up to distances of at least 90 m. The scale radius for $E_{\text{th}} \geq 50$ GeV is $r_h \simeq 10$ m and scales roughly proportional to E_{th}^{-1} , as expected by a simple dimensional comparison of electromagnetic multiple scattering and hadronic interactions.
- The interrelation between the electromagnetic and hadronic EAS component may explain the ‘unconventional’ small preferred scale radius of the electron LDF of 20-30 m as compared to the classical value of $r_M \simeq 80$ m. It should be kept in mind that the classical Molière radius has been derived for pure electromagnetic showers and for zero energy threshold only. However, extensive air showers are mostly initiated by primary hadrons. Therefore,

the shower evolution is mostly driven by the substantially narrower hadronic component, and the effective lateral scale radius of observed electrons is expected to be smaller than for $E_{\text{kin}} \geq 0$ electrons in pure γ -initiated showers.

The present paper is not focussed to detailed analyses in terms of predictions of the EAS developments from Monte Carlo simulations and to a comparison of different theoretical high-energy interaction approaches like VENUS [35], QGSJET [29] and SIBYLL [36]. These models, continuously in the process of refinement, are generators implemented into the Karlsruhe EAS Monte Carlo code CORSIKA [27]. However, the presented results provide a coherent experimental basis for serious tests considering simultaneously the three main EAS components, not only concerning the interaction but also the particle propagation procedures. It may be noted that the muon lateral distributions are experimentally given for three different energy detection thresholds of the registered muons, thus implying also some sensitivity to the low energy spectrum. Most valuable for such tests are observations based on the hadronic component. An example of first analyses in this scope were presented in [37] and a remarkable agreement of lateral distributions of hadrons for primary protons and Fe nuclei was observed. In particular, the absence of peculiar features, in contrast to earlier observations by Danilova et al. [16] and Arvela and Elo [18] can be stated, even at energies as high as 10 PeV. Such results support the trust in a correct handling of the particle propagation and of the development of the hadronic component at least for hadron energies above 50 GeV. More detailed comparisons of lateral distributions with CORSIKA simulations are under study and will be subject of a forthcoming publication.

Acknowledgements

The authors are indebted to the members of the engineering and technical staff of the KASCADE collaboration, who contributed with enthusiasm and engagement to the success of the experiment.

The support, based on common projects of Scientific-Technological Cooperation Agreements (WTZ) and provided by the Ministry for Research of the German Federal Government and International Bureau Bonn, is gratefully acknowledged. The collaboration has been partly supported by grants of the Polish Committee for Scientific Research, the Romanian Ministry of Research and Technology, of the Armenian Government and an ISTC project (A116).

References

- [1] P. Auger et al., *Rev. Mod. Phys.* 11 (1939) 288.
- [2] K. Greisen, *Ann. Rev. Nucl. Sci.* 10 (1960) 63.

- [3] K. Kamata and J. Nishimura, *Prog. Theoret. Phys. Suppl.* 6 (1958) 93.
- [4] J. Nishimura, *Handbuch der Physik*, volume 46/2, pp. 1–114, Springer-Verlag, 1967.
- [5] S. Yoshida et al., *J. Phys. G: Nucl. Part. Phys.* 20 (1994) 651.
- [6] A. V. Glushkov et al., *Proc. 25th ICRC*, Durban, Vol. 6, p. 233, 1997.
- [7] R. N. Coy et al., *Astroparticle Physics* 6 (1997) 263.
- [8] A. M. Hillas and J. Lapikens, *Proc. 15th ICRC*, Plovdiv, Vol. 8, p. 460, 1977.
- [9] J. N. Capdevielle, J. Gawin, and J. Procureur, *Proc. 15th ICRC*, Plovdiv, Vol. 8, p. 341, 1977.
- [10] A. A. Lagutin et al., *Proc. 25th ICRC*, Durban, Vol. 6, p. 285 and p. 289, 1997.
- [11] R. Armitage et al., *J. Phys. G* 13 (1987) 707.
- [12] N. Hayashida et al., *J. Phys. G* 21 (1995) 1101.
- [13] M. Aglietta et al., *Nuovo Cimento B* 112B (1997) 139.
- [14] J. Linsley, *Proc. 8th ICRC*, Jaipur, Vol. 4, p. 77, 1963.
- [15] A. M. Hillas et al., *Proc. 11th ICRC*, Budapest, Vol. 3, p. 533, 1969; *Acta Physica Academiae Scientiarum Hungaricae* 29, Suppl. 3, pp. 533-538, 1970.
- [16] T. V. Danilova et al., *Proc. 19th ICRC*, La Jolla, Vol. 7, p. 40, 1985.
- [17] H. Hasegawa et al., *Proc. 9th ICRC*, London, Vol. 2, p. 642, 1965.
- [18] H. Arvela and A.-M. Elo, *Proc. 24th ICRC*, Rome, Vol. 1, p. 332, 1995.
- [19] R. H. Vatcha and B. V. Sreekantan, *J. Phys. A* 6 (1973) 1050.
- [20] R. H. Vatcha and B. V. Sreekantan, *J. Phys. A* 6 (1973) 1067.
- [21] G. Cocconi, *Handbuch der Physik*, volume 46/1, pp. 215–271, Springer-Verlag, 1961.
- [22] S. V. Ter-Antonian et al., *Proc. 24th ICRC*, Rome, Vol. 1, p. 369, 1995.
- [23] R. Ticona et al., *Proc. 23rd ICRC*, Calgary, Vol. 4, p. 331, 1993.
- [24] P. Doll et al., (KASCADE Collaboration), *The Karlsruhe cosmic ray project KASCADE*, Report KfK 4686, Kernforschungszentrum Karlsruhe, 1990.
- [25] H. O. Klages et al., (KASCADE Collaboration), *Nucl. Phys. B, Proc. Suppl.* 52B (1997) 92.
- [26] J. Engler et al., *Nucl. Instr. and Meth. A* 427 (1999) 528.
- [27] D. Heck et al., *CORSIKA: A Monte Carlo code to simulate extensive air showers*, Report FZKA 6019, Forschungszentrum Karlsruhe, 1998.
- [28] J. Weber et al., (KASCADE Collaboration), *Proc. 25rd ICRC*, Durban, Vol. 6, p.153, 1997.
- [29] N.N. Kalmykov, S.S. Ostapchenko, A.I. Pavlov, *Nucl. Phys.* 52B (1997) 17.
- [30] Application Software Group, *GEANT - Detector Description and Simulation Tool*, CERN, Geneva, 1993.
- [31] H.H. Mielke, *Internal Report FZK 51.02.03-01*, Forschungszentrum Karlsruhe, 1996

- [32] R. Glasstetter et al., (KASCADE Collaboration), Proc. 26rd ICRC, Salt Lake City, Vol. 2, p.222, 1999.
- [33] A. Haungs et al., (KASCADE Collaboration), Features of the EAS muon density distributions measured with the KASCADE experiment, Report FZKA 6263, Forschungszentrum Karlsruhe, 1999.
- [34] J. Kempa, Nuovo Cimento 31A (1976) 568 and 581.
- [35] K. Werner, Physics Reports 232 (1993) 87.
- [36] R.S. Fletcher et al., Phys. Rev. D 50 (1995) 5710.
- [37] T. Antoni et al., (KASCADE Collaboration), J. Phys. G 25 (1999) 2161.